HHS Public Access

Author manuscript

Nat Med. Author manuscript; available in PMC 2012 November 01.

Published in final edited form as:

Nat Med. ; 18(5): 829–834. doi:10.1038/nm.2721.

A Brain Tumor Molecular Imaging Strategy Using A New Triple-Modality MRI-Photoacoustic-Raman Nanoparticle

Moritz F Kircher[1,2,3,4,15], **Adam de la Zerda**[1,5,15], **Jesse V Jokerst**[1], **Cristina L Zavaleta**[1], **Paul J Kempen**[6], **Erik Mittra**[1], **Ken Pitter**[4,7], **Ruimin Huang**[2,4,8], **Carl Campos**[9], **Frezghi Habte**[1], **Robert Sinclair**[6], **Cameron W. Brennan**[4,9,10,11], **Ingo K Mellinghoff**[8,9,12], **Eric C Holland**[4,7,8,10,11,13], and **Sanjiv S Gambhir**[1,6,14]

[1]Molecular Imaging Program at Stanford, Department of Radiology, Stanford University, Stanford, California, USA

[2]Department of Radiology, Memorial Sloan-Kettering Cancer Center, New York, New York, USA

[3]Department of Radiology, Weill-Cornell Medical College, New York, New York, USA

[4]Brain Tumor Center, Memorial Sloan-Kettering Cancer Center, New York, New York, USA

[5]Department of Electrical Engineering, Stanford University, Stanford, California, USA

[6]Department of Materials Science & Engineering, Stanford University, Stanford, California, USA

[7]Department of Cancer Biology and Genetics, Memorial Sloan-Kettering Cancer Center, New York, New York, USA

[8]Department of Neurology, Memorial Sloan-Kettering Cancer Center, New York, New York, USA

[9]Human Oncology & Pathogenesis Program, Memorial Sloan-Kettering Cancer Center, New York, New York, USA.

[10]Department of Neurosurgery, Memorial Sloan-Kettering Cancer Center, New York, New York, USA

[11]Department of Neurosurgery, Weill-Cornell Medical College, New York, New York, USA

[12]Department of Pharmacology, Weill-Cornell Medical College, New York, New York, USA

[13]Department of Surgery, Memorial Sloan-Kettering Cancer Center, New York, New York, USA

Corresponding Author: Sanjiv S Gambhir, MD PhD, The James H Clark Center, 318 Campus Drive, Stanford, CA 94305-5427, sgambhir@stanford.edu, Fax: 650-724-4948.

[15]These authors contributed equally to this work.

Author Contributions

M.F.K. co-initiated the project, designed the research, synthesized and characterized MPR nanoparticles, performed MRI, Raman, Photoacoustic and histology experiments, analyzed data, and wrote the manuscript. A.D. modified the Photoacoustic system, designed and performed Photoacoustic experiments, analyzed data, and wrote the manuscript. J.V.J. synthesized and characterized MPR nanoparticles. C.L.Z. designed, performed and analyzed Raman experiments and edited the paper. P.J.K. and R.S. performed and analyzed electron microscopy experiments. K.P. performed immunohistochemistry. F.H. helped create 3D renderings. E.M., M.F.K., K.P., R.H., C.C., C.W.B., I.K.M. and E.C.H. provided mouse models. S.S.G. co-initiated the project, designed the research, analyzed data, supervised and coordinated all investigators for the project, and wrote the manuscript.

[14]Department of Bioengineering and Bio-X Program, Stanford University, Stanford, California, USA

Abstract

The vexing difficulty in delineating brain tumor margins represents a major obstacle toward better outcome of brain tumor patients. Current imaging methods are often limited by inadequate sensitivity, specificity, and spatial resolution. Here we show that a unique triple-modality Magnetic resonance imaging - Photoacoustic imaging – surface enhanced Raman scattering (SERS) nanoparticle (MPR) can accurately help delineate the margins of brain tumors in living mice both pre- and intra-operatively. The MPRs were detected by all three modalities with at least picomolar sensitivity both *in vitro* and in living mice. Intravenous injection of MPRs into glioblastoma-bearing mice led to specific MPR accumulation and retention by the tumors, allowing for non-invasive tumor delineation by all three modalities through the intact skull. Raman imaging allowed guidance of intra-operative tumor resection, and histological correlation validated that Raman imaging is accurately delineating brain tumor margins. This novel triple-modality nanoparticle approach holds promise to enable more accurate brain tumor imaging and resection.

Keywords

MRI; Photoacoustic; Raman; SERS; multimodality; nanoparticle; molecular imaging; brain tumor; tumor margin; in vivo; contrast agent; cancer; surgery; gold; silica

Introduction

The completeness of the surgical resection is an important factor for the prognosis of brain tumor patients[1,2]. In trying to achieve more complete glioma resections, the surgeon encounters several hurdles, which include irregular and indistinct tumor margins as well as tumor growth adjacent to or invading crucial neurological structures[3]. A wide variety of techniques have been explored to date in an effort to better visualize tumor margins. For instance, pre-operative magnetic resonance imaging (MRI) has been used to guide stereotactic surgery, where the MR images are used to determine the macroscopic outline of the tumor[4]. However, such methods suffer from limited spatial resolution and incongruencies between pre-operative MRI and actual tumor borders during surgery due to brain shift[5]. Intra-operative MRI usually requires the administration of gadolinium (Gd)-chelates, which suffer from short blood half-life requiring repeated injections[6], high dosages[7] and inaccuracies due to surgically induced false-positive contrast enhancement[8]. Several intra-operative optical methods have been suggested, either based on intrinsic tissue optical properties[3,9] or exogenous contrast agents[10–12]. However, these optical techniques suffer from poor specificity due to tissue autofluorescence, limited resolution and depth of penetration, which ultimately limit localization of the true brain tumor margins[13,14].

Photoacoustic imaging is a novel technology that largely overcomes the depth and resolution limits of optical imaging. In Photoacoustic imaging, light pulses excite target molecular imaging agents causing very slight heat production. This produces ultrasound waves that are

recorded by an ultrasound transducer leading to a three-dimensional image of the imaging agent distribution in living subjects[15,16]. Raman imaging, another promising and complementary optical imaging technique, can be greatly enhanced by the Surface Enhanced Raman Scattering (SERS) effect[17]. Due to the unique signature of the SERS spectrum, Raman imaging allows for highly specific and sensitive detection of SERS contrast agents as well as the multiplexing of multiple agents in living subjects[17–20].

An ideal molecular imaging agent would be 1) sequestered and retained by a tumor for a long enough period such that a single injection of the agent would facilitate 2) both pre- and intra-operative imaging allowing for respective pre-operative planning and intra-operative resection of the tumor. It should also allow for both 3) deep tumor visualization and 4) highly sensitive and specific detection of tumor margins.

Here we present a novel approach that attempts to fulfill these criteria. We have designed and tested MPRs for a triple-modality strategy that, to our knowledge, is the first to allow combined MRI, Photoacoustic imaging and Raman imaging. After a single tail-vein injection into orthotopic mouse glioblastoma models, the MPRs accumulated in the tumor but not in healthy brain tissue due to the enhanced permeability and retention (EPR) effect[21] (Fig. 1). The particles resided in the tumor for an extended period of time (≥ 1 week) and were detected with all three modalities in living mice with at least picomolar sensitivity. This allowed 1) whole brain tumor localization for pre- and intra-operative macroscopic delineation using MRI, 2) high spatial resolution, three-dimensional imaging using Photoacoustic imaging, and 3) high sensitivity, high specificity and high resolution surface imaging of tumor margins using Raman imaging. Moreover, excised tissues may be further analyzed post-operatively using Raman imaging to confirm clear margins (Fig. 1).

Results

Synthesis and characterization of triple-modality MPRs

The MPR nanoparticle is composed of a 60 nm gold core covered with the Raman molecular tag, trans-1,2-bis(4-pyridyl)-ethylene. This thin Raman-active layer is further protected by a 30 nm silica coating. We further modified the particles with DOTA-Gd^{3+} via a maleimide linkage (see Methods), resulting in a gold-silica-based SERS nanoparticle coated with Gd^{3+} ions (MPR) (Fig. 2a, b). We determined the number of Gd^{3+} ions per MPR to be 79,340 ± 2,270 via inductively coupled plasma atomic emission spectroscopy (ICP-AES). A portion of these Gd^{3+} ions could be bound directly to the silica surface. To test the serum stability of the MPRs we performed ICP-AES and found that the number of Gd^{3+} ions per MPR did not significantly decrease in the presence of serum after 2 h or 24 h of incubation (data not shown). In addition, we validated that the MPRs are stable in serum by measuring their optical stability (Supplementary Fig. 1) and hydrodynamic size distribution (Supplementary Fig. 2) over a course of 24 h of incubation in mouse serum. The stable binding of Gd^{3+} ions to the nanoparticle surface and absence of any free Gd^{3+} ions in solution was verified by acquiring T1-weighted MR images of the supernatant after particle centrifugation (data not shown). The MPRs demonstrated a very high T1 relaxivity of 3.0×10^6 mM^{-1} s^{-1} (in H_2O, at a field strength of 7 T and 20 °C), with minimal batch-to-batch variation (see error bars in Fig. 2c). The MPR optical absorbance peaked at 540 nm, with a very high absorbance

coefficient of 2.75×10^{10} $cm^{-1}M^{-1}$ (Fig. 2d). We therefore further modified our custom-made Photoacoustic imaging system to include a 532 nm laser to allow imaging of the MPRs (see Supplementary Methods). The MPRs demonstrated a unique Raman signature (Fig. 2e), which was identical before and after the surface conjugation of the maleimide-DOTA-Gd to the particle (Supplementary Fig. 3). To test for possible photobleaching, we irradiated the MPRs in both the Photoacoustic and Raman imaging systems. During 30 min of continuous laser irradiation, the optical absorption and Raman signal did not vary more than 2% each (Fig. 2f, g, and Supplementary Methods).

In vitro and *in vivo* detection of MPRs by MR, Photoacoustic and Raman Imaging

Next, we determined the *in vitro* detection threshold of the MPRs for each modality. An agarose phantom containing MPRs in concentrations ranging from 1.22 pM to 1250 pM (n = 3 per concentration) was imaged with MRI, Photoacoustic and Raman (Supplementary Fig. 4a), and signal intensities were determined by region of interest (ROI) analysis (Supplementary Fig. 4b). The lowest detectable concentrations were 4.88 pM for MRI, 1.22 pM for Photoacoustic, and 610 fM for Raman imaging (see Supplementary Fig. 5). The MRI, Photoacoustic and Raman signals produced by MPRs *in vitro* were highly correlated to the MPR concentration ($P < 0.0001$ for all modalities, with R^2 = 0.97, 0.99 and 0.99, respectively) (Supplementary Fig. 4b) and were further highly linear and correlated to each other (see Supplementary Fig. 6). For a comparison of the depth of penetration of Photoacoustic imaging versus Raman imaging, see Supplementary Figure 7.

We then measured the detection threshold of the MPRs in living mice. All animal experiments were performed in compliance with the Guidelines for the Care and Use of Research Animals established by the Stanford University Animal Studies Committee. MPRs diluted in matrigel to six different concentrations (range 50 pM to 1100 pM) were injected subcutaneously in the right flank of nude mice (n = 3) and scanned in the MRI, Photoacoustic and Raman systems (Supplementary Fig. 8a). The MRI, Photoacoustic and Raman signals *in vivo* highly correlated to the MPR concentration (P = 0.001 for all modalities, with R^2 = 0.99, 0.97 and 0.99, respectively) (Supplementary Fig. 8b). Due to the high background signal, the sensitivity of MRI and Photoacoustic imaging was limited by the tissue background signal. For both MRI and Photoacoustic imaging, 50 pM of MPRs gave the equivalent signal as muscle. Raman imaging, however, had negligible tissue background signal, and was therefore limited only by the signal-to-noise ratio. Indeed, at the nominal concentration of 50 pM, the Raman image clearly visualized the MPRs. This explains why the Raman response had the steepest slope *in vivo* compared to MRI and Photoacoustic imaging ($P < 0.0001$ compared to either MRI or Photoacoustic imaging; however, the slope of Photoacoustic imaging was not statistically different from the MRI slope, P = 0.16), whereas *in vitro*, where no significant background signal is present, Photoacoustic imaging has the steepest slope. Finally, a linear correlation between the signals of the three modalities was observed (Supplementary Fig. 9).

MPRs allow triple-modality brain tumor visualization in intact living mice

We next aimed at determining whether the MPRs could be used for orthotopic brain tumor detection in living mice. We hypothesized that in an orthotopic glioblastoma brain tumor

model the nanoparticle probe would enter the extravascular space due to diffusion through the disrupted blood-brain-barrier and accumulate in cells within the tumor without necessitating a specific targeting mechanism (EPR effect), as previously observed for iron oxide nanoparticles[22]. We used an orthotopic brain tumor model where enhanced green fluorescent protein (eGFP)-transfected human gliomablastoma cells (eGFP+U87MG) were implanted via a stereotactic implantation device into the striatum of nude mice (Supplementary Methods). We injected tumor-bearing mice (n = 4) via tail-vein with MPRs and performed consecutive Photoacoustic, Raman and MR imaging on each animal pre-injection and at 2 h, 3 h and 4 h post-injection, respectively (Fig. 3; Supplementary Fig. 10).

The post-injection images demonstrated clear visualization of the tumor with all three modalities, despite being acquired through intact skin and skull (Fig. 3a). The Photoacoustic and Raman images were co-registered with the MRI image, demonstrating good co-localization between the three modalities (Fig. 3a). In parallel to the Photoacoustic images of the brain, we also acquired co-registered ultrasound images in order to register the Photoacoustic images to the MR images in orthogonal planes (Fig. 3b) (using Amide[23] and Amira software, see Supplementary Methods).

ROI quantification of the signal in the tumor shows a significant increase in MRI, Photoacoustic and Raman signals after the tail-vein injection versus before (Fig. 3c). The MRI contrast-to-noise ratio (CNR) increased from 2.2±0.3 to 14.0±1.9 (mean±S.E.) (P = 0.001). The Photoacoustic signal increased by 75% from 0.57±0.02 to 1.0±0.08 (arbitrary units (AU)) (P = 0.001). The Raman system recorded zero signal before the injection, and an intense Raman signal of 1.0±0.09 (AU) (P = 0.012) after injection.

We then determined the molecular imaging agent kinetics with all three modalities using additional orthotopic eGFP+U87MG tumor-bearing mice (n = 4 each for MRI and Raman imaging; the Photoacoustic data was derived from the first set of mice described in Fig. 3). We analyzed the signal kinetics for each of the mice individually in the MRI, Photoacoustic and Raman imaging systems (Supplementary Fig. 11). We acquired data before injection and at 0.5 h, 1 h, 1.5 h and 2 h post-injection. For MRI, an additional 24 h time point was acquired. The signal was observed to increase markedly between the pre-injection and the 30 min post-injection time points in all three modalities (from 1.4±0.24 to 8.7±0.76 CNR for MRI (P < 0.001), 60±14% increase for Photoacoustic imaging (P < 0.01), and from zero to 1.96±0.27 (AU) for Raman imaging (P < 0.001). The signal then reached a plateau for MRI and Photoacoustic, remaining essentially stable up to the latest examined time point of 2 h (24 h for MRI). Of note, this behavior contrasts with conventional clinically used Gd-based contrast agents, which demonstrate rapid washout within minutes after injection, while the MPRs demonstrate persistent signal enhancement (Supplementary Fig. 11). For Raman, an initial signal peak was observed, before a plateau was reached (P < 0.0001). This effect is presumed due to initial nonspecific circulation of MPRs in superficial layers (e.g. skin), to which Raman is most sensitive (Supplementary Fig. 11).

Histological validation of MPR sequestration by brain tumors

We next examined the distribution of the MPRs within the brain by histology. We performed immunohistochemistry with antibody staining against eGFP and CD11b to

visualize eGFP+U87MG tumor cells and microglia, respectively. In particular, we sampled sections including the interface between tumor and surrounding brain tissue. We then examined adjacent sections with high-resolution Raman microscopy (Supplementary Methods) and correlated these images with the immunohistochemistry results. We observed a strong Raman signal within the tumors, but not in healthy brain tissue, with very good delineation of the actual tumor border by the Raman signal (Fig. 4). Scanning transmission electron microscopy (STEM) (Fig. 4) further corroborated these results, finding numerous MPRs in tumor sections, while none were found in surrounding brain tissue (923 MPRs found in tumor in an examined volume of 57,500 μm^3 (average of 0.016 nanoparticles/μm^3), 0 nanoparticles found in healthy brain in an examined volume of 12,500 μm^3). A three-dimensional STEM rendering of MPRs in tumor is provided in the Supplementary Information as Supplementary Movie.

To further examine the ability of the MPRs to visualize not only the bulk tumor, but also invasive tumor margins, we used an orthotopic primary human xenograft glioblastoma mouse model (TS543 cell line[24] grown as neurospheres). As confirmed by correlative Raman microscopy, immunohistochemistry, and scanning electron microscopy (SEM), the MPRs accumulated in infiltrating tumor margins (Supplementary Fig. 12). In addition, Raman imaging was able to depict finger-like tumor protrusions and even isolated microscopic tumor foci (Supplementary Fig. 13).

MPRs guide brain tumor resection *in vivo*

Finally, we explored whether tumor resection along the Photoacoustic and Raman signals, 24 h after intravenous injection of MPRs, could facilitate tumor resection. Initially, we tested the ability of Photoacoustic imaging to delineate brain tumors *in situ*, which demonstrated a reduced signal in the resected area (Supplementary Fig. 14). Next, we placed brain tumor-bearing mice (n = 3) under general anesthesia and performed craniotomies and subsequent *in vivo* Raman imaging. Sections of the brain tumors were then removed using visual inspection. High-resolution intra-operative Raman images after each resection step were obtained and correlated with intra-operative photographs. The whole tumor was visualized with Raman imaging (first image in 5a,b). With sequential resection steps, a high congruency between residual tumor tissue (Fig. 5a) and presence of Raman signal (Fig. 5b) was noted, and *vice versa* between resected tumor and lack of Raman signal. Of note, after the tumor resection appeared complete using visual inspection, several small foci of residual Raman signal (dashed box in Fig. 5b) were noted in the resection bed. When we then extended the resection to include these foci located near the tumor-brain interface and histologically analyzed this tissue, we found frequent finger-like microscopic extensions of tumor into the surrounding brain tissue (Fig. 5c). These cancerous foci, which were otherwise not visible by the naked eye, were detected due to the specific accumulation of the MPRs therein.

Discussion

We designed and tested a unique triple-modality nanoparticle that is, to our knowledge, the first to allow combined MRI, Photoacoustic and Raman imaging. The MPRs described here

could enable radiologists and neurosurgeons to “see” the same probe before and during surgery, thus allowing more accurate brain tumor resection by exploiting the complementary strengths of each modality.

The excellent MRI detectability of the MPRs in the picomolar range is a direct result of their very high longitudinal relaxivity of 3.0×10^6 mM^{-1} s^{-1}. To our knowledge, this represents the highest relaxivity of a nanoparticle reported to date.

The second modality, Photoacoustic imaging, is a relatively new technique that allows deeper tissues to be imaged with higher spatial resolution compared to most optical techniques[25–27]. The exceptionally high optical absorbance coefficient of the MPRs is over 200-fold higher than, for example, previously reported Photoacoustic imaging agents based on carbon nanotubes[28,29]. In conjunction with its three-dimensional capabilities, Photoacoustic imaging could guide the more gross resection steps and even identify tumor tissue residing under the surface of normal brain tissue. Then, to completely remove microscopic tumor deposits, Raman imaging with its superior sensitivity could be employed.

Raman spectroscopy in conjunction with MPRs offers ultrahigh sensitivity in the picomolar range as opposed to the nanomolar sensitivity achievable with fluorescence imaging of quantum dots[13,17,18,20]. Raman imaging of MPRs, in contrast to other optical imaging techniques, does not suffer from autofluorescence or background signal because the MPR spectral signature is highly amplified and unique (“fingerprint”). While the main limitation of Raman imaging is its limited penetration depth, tumor visualization was achieved in our study through the intact skin and skull in live mice (depth of 2–5 mm). This result is a combination of the design of the nanoparticle with its gold core producing a surface plasmon resonance for Raman signal enhancement; the Raman substrate used; and the number of nanoparticles accumulating within the tumor. Raman nanoparticles are inherently insensitive to photodestruction, which represents a known problem of organic fluorochromes. Furthermore, unlike most quantum dots, which are cytotoxic[30,31], MPR nanoparticles are based on inert gold and silica and thus may have a better chance for clinical translation. Gold and gold-silica nanoparticles have excellent cytotoxicity profiles, as illustrated by detailed toxicity studies in animals[32–34] and several clinical trials[21]. The design of the MPRs would also allow for multiplexing[20] with the potential to detect multiple biomarkers simultaneously *in vivo*.

In addition, MPRs have a unique advantage over conventional low molecular weight contrast agents. For example, low molecular weight Gd-chelates or fluorochromes accumulate in the extracellular space, where blood-brain-barrier breakdown has occurred, and then undergo both rapid diffusion through the interstitium and renal clearance. These low molecular weight agents are therefore unable to delineate tumors for the time period spanning the resection procedure, let alone for the entire period between pre-operative planning and surgical intervention. This diffusion process also introduces imprecision of probe localization, requires repeated contrast administration (e.g. Gd-chelates during intra-operative MRI), and can cause false positive results due to surgically induced contrast enhancement. In contrast, the *in vivo* kinetic studies performed with the MPRs here demonstrate that the particle is being retained in the tumor, allowing repeated imaging as

required without the need for repeated injection. This contrast agent behavior may also be useful for distinguishing tumor recurrence from non-specific treatment-related effects. As the MPR approach relies on the EPR effect, it could potentially be applied to image other cancer types with intrinsic EPR effect including: lung cancer, melanoma, renal cancer, hepatoma, and many others [35]. Finally, the long intratumoral retention of the MPRs could also be exploited for drug delivery or photothermal therapy.

Novel instrumentation, including endoscopic and intra-operative Photoacoustic and Raman imaging devices required for clinical translation of the MPR approach, are currently under development[36,37]. Ideally, a combination of both devices integrated in one handheld probe would be desirable in the operating room. In particular, such endoscopes should be designed for easy intra-operative navigation and enable real-time imaging. Further development of instrumentation could lead to improved brain tumor surgery and patient outcome in the future. For additional discussion, please refer to the Supplementary Discussion section in the Supplementary Information.

Methods

Particle synthesis

Reagents—SERS nanotags (Cabot Security Materials, Inc.) comprised a 60 nm diameter gold core coated with a monolayer of a Raman-active organic molecule, trans-1,2-bis(4-pyridyl)-ethylene, and encapsulated with a 30 nm diameter silica shell, making the entire particle on the order of ~120 nm. We purchased phosphate buffered saline, 2-(N-morpholino)ethanesulfonic acid (MES), 3-mercaptopropyl-trimethoxysilane (MPTMS), gadolinium chloride hexahydrate, and sodium chloride from Sigma-Aldrich, 5,5'-dithio-bis(2-nitrobenzoic acid) (DTNB, Ellman's reagent) from Pierce and 1,4,7,10-tetraazacyclododecane-1,4,7-tris-acetic acid-10-maleimidoethylacetamide (maleimide-DOTA) from Macrocyclics.

Bioconjugation—We activated the SERS nanotag surface with 10 mM MES buffer of pH 7.0 for binding of maleimide-DOTA to the mercaptopropyl trimethoxysilane (MPTMS)-coated surface. We added the DOTA chelator at a molar excess of 7.5×10^5 per nanoparticle from a stock solution of 1 mg/mL, reacted for 2 h at room temperature (RT) and removed excess reagent via centrifugation (5,000 g × 5 min) × 3. We added gadolinium chloride hexahydrate (3 mg/mL) to the DOTA-activated nanoparticles in MES buffer (pH 6.25), with a ratio of Gd to nanoparticle of 7.5×10^5 : 1. We heated this solution to 50 °C for 2 h, washed × 3 as above, and then purified by dialysis versus distilled water and a 3.5 kDa molecular weight cutoff membrane. Optical absorbance was measured using a UV-Vis spectrophotometer (DU-640 spectrophotometer, Beckman Coulter).

MRI

We conducted MRI scans with a dedicated small animal MRI scanner, custom-designed pulse sequences and radiofrequency (RF) coils. The small animal scanner consisted of a superconducting magnet (Magnex Scientific) with 7.0 Tesla (T) field strength, gradient (Resonance Research, Inc.) with clear bore size of 9 cm, maximum gradient amplitude of

770 mT/m and maximum slew rate of 2,500 T/m/s and a General Electric (GE) console and Copley 266 amplifiers.

We obtained T1-weighted fast spin echo sequences (TE/TR 7.7 ms / 800 ms) using 5 NEX, a 256 × 256 matrix, a 3.0 cm field-of-view (resulting in an in-plane resolution of 117 μm), a slice thickness of 700 μm and a total imaging time of ~4 min. For acquisition of T1 maps, we used an inversion recovery sequence (TE/TR 7.7 ms / 5,000 ms) with inversion times of 50, 100, 200, 500, 800, 1200 and 2100 ms. We obtained estimates of T1 relaxation times by fitting the acquired inversion recovery images to a function of the form $S=M_0\left|1-2e^{-\frac{T1}{T1}}+e^{-\frac{TR}{T1}}\right|$ (Reference [38]). We performed data fitting using a non-linear least squares algorithm implemented in the RT_Image[39] analysis software. We obtained T2-weighted fast spin echo sequences (TE/TR 71 ms / 4,000 ms) using 4 NEX, a 256 × 128 matrix, a 3.0 cm field-of-view, a slice thickness of 700 μm and a total imaging time of ~3.5 min.

Raman imaging of living mice

To measure Raman signal, we used a customized Raman microscope (InVia, Renishaw). Since previous reports[18,20], we further customized the microscope by integrating a 785 nm point source laser, piezo-controlled stage for micron-resolved spatial mapping, and a 1 inch charge-coupled device detector for spectral resolution of 1.07 cm^{-1}. We carefully positioned living mice into a nose cone under the microscope and anesthetized with 2–3% isoflurane delivered by 100% oxygen as the carrier gas at 2 L/min through an isoflurane vaporizer. We used a semiconductor diode near-infrared laser operating at 785 nm as the excitation source with a laser power of ~20 mW measured at the skin surface. We obtained Raman images by using a Raman point mapping method. We used a computer-controlled x-y translation stage to raster-scan over the brain, using an integration time of 1–5 s, a 5× or 12× lens, a slit size of 400 μm, and either a 750 μm or 500 μm step size. Raman spectra were analyzed with Wire 2.0 Software (Renishaw) and Nanoplex™ SENSERSee software (provided by Cabot Security Materials, Inc.)

Photoacoustic imaging system

Our custom-built Photoacoustic system[15] is illustrated in Supplementary Figure 16. A tunable pulsed laser with a repetition rate of 10 Hz and a pulse width of 5 ns (Nd:YAG Surelight-III-10, Continuum) illuminates the object through a fiber optic ring light (50-1353 Ringlight, Fiberoptic Systems Inc.). The average energy density of the laser at 532 nm was ~ 8 mJ/cm^2 on the tissue surface, which is below the limitation for laser skin exposure defined by the American National Standards Institute[40]. We used a 5 MHz focused transducer (A309S-SU-F-24.5-MM-PTF; 25.5 mm focal length, 4 MHz bandwidth, f-number of 2.0, depth of focus of 6.5 mm, lateral resolution of 600 μm, and axial resolution of 380 μm; Panametrics-Olympus NDT) to acquire both pulse-echo and Photoacoustic images. In addition, we acquired high-resolution ultrasound images using a 25 MHz focused transducer (V324-SU-25.5-MM; 27 mm focal length, 12 MHz bandwidth, F number of 4.2, depth of focus of 7.5 mm, lateral resolution of 250 μm, and axial resolution of 124 μm; Panametrics-Olympus NDT).

Supplementary Material

Refer to Web version on PubMed Central for supplementary material.

Acknowledgements

The authors would like to thank M. Gozin for help with ICP, L. Pisani for assistance with quantifying and acquiring MR data, S. M. Korn and S. Bodapati for assistance in conducting the Photoacoustic experiments, J. Rosenberg for assistance with statistical analysis, and the MSKCC Small Animal MRI Imaging core (J. Koutcher and C. C. Le) for technical assistance. M. Kircher would like to thank R. Herfkens and the Stanford Department of Radiology for providing academic time to perform the study. We would like to acknowledge the following funding sources: National Cancer Institute grants CCNE U54 CA119367 (S.S.G.), CCNE U54 U54CA151459 (S.S.G.), and ICMIC P50 CA114747 (S.S.G.); The Ben and Catherine Ivy Foundation (S.S.G.); the Canary Foundation (S.S.G.), the Sir Peter Michael Foundation (S.S.G.), the Bio-X Graduate Student Fellowship (A.D.); the Department of Defense Breast Cancer Research Program – Pre-doctoral Traineeship Award BC083014 (A.D.) and the NCI SMIS R25T Fellowship 5R25CA118681 (J.V.J.).

The authors would also like to thank T.F. Massoud, D. Akin, H.E. Daldrup-Link, S. Bohndiek, S. Harmsen and J. Samii for critical review of the manuscript and B.T. Khuri-Yakub, S. Vaithilingam, O. Oralkan, E.E. Graves, and H. Fan-Minogue for helpful discussions.

References

1. Bucci MK, et al. Near complete surgical resection predicts a favorable outcome in pediatric patients with nonbrainstem, malignant gliomas: results from a single center in the magnetic resonance imaging era. Cancer. 2004; 101:817–824. [PubMed: 15305415]
2. Stupp R, et al. Changing paradigms--an update on the multidisciplinary management of malignant glioma. Oncologist. 2006; 11:165–180. [PubMed: 16476837]
3. Toms SA, et al. Intraoperative optical spectroscopy identifies infiltrating glioma margins with high sensitivity. Neurosurgery. 2005; 57:382–391. discussion 382–391. [PubMed: 16234690]
4. Orringer DA, et al. The brain tumor window model: a combined cranial window and implanted glioma model for evaluating intraoperative contrast agents. Neurosurgery. 2010; 66:736–743. [PubMed: 20305495]
5. Reinges MH, et al. Course of brain shift during microsurgical resection of supratentorial cerebral lesions: limits of conventional neuronavigation. Acta Neurochir (Wien). 2004; 146:369–377. discussion 377. [PubMed: 15057531]
6. Ludemann L, Hamm B, Zimmer C. Pharmacokinetic analysis of glioma compartments with dynamic Gd-DTPA-enhanced magnetic resonance imaging. Magn Reson Imaging. 2000; 18:1201–1214. [PubMed: 11167040]
7. Knauth M, Wirtz CR, Aras N, Sartor K. Low-field interventional MRI in neurosurgery: finding the right dose of contrast medium. Neuroradiology. 2001; 43:254–258. [PubMed: 11305762]
8. Knauth M, et al. Surgically induced intracranial contrast enhancement: potential source of diagnostic error in intraoperative MR imaging. AJNR Am J Neuroradiol. 1999; 20:1547–1553. [PubMed: 10512244]
9. Beljebbar A, Dukic S, Amharref N, Manfait M. Ex vivo and in vivo diagnosis of C6 glioblastoma development by Raman spectroscopy coupled to a microprobe. Anal Bioanal Chem. 2010; 398:477–487. [PubMed: 20577720]
10. Ozawa T, et al. Bromophenol blue staining of tumors in a rat glioma model. Neurosurgery. 2005; 57:1041–1047. discussion 1041–1047. [PubMed: 16284574]
11. Shinoda J, et al. Fluorescence-guided resection of glioblastoma multiforme by using high-dose fluorescein sodium. Technical note. J Neurosurg. 2003; 99:597–603. [PubMed: 12959452]
12. Stummer W, et al. Fluorescence-guided surgery with 5-aminolevulinic acid for resection of malignant glioma: a randomised controlled multicentre phase III trial. Lancet Oncol. 2006; 7:392–401. [PubMed: 16648043]
13. de la Zerda A, et al. A comparison between time domain and spectral imaging systems for imaging quantum dots in small living animals. Mol Imaging Biol. 2010; 12:500–508. [PubMed: 20012220]

14. Kantelhardt SR, et al. Multiphoton excitation fluorescence microscopy of 5-aminolevulinic acid induced fluorescence in experimental gliomas. Lasers Surg Med. 2008; 40:273–281. [PubMed: 18412229]
15. de la Zerda A, et al. Carbon nanotubes as photoacoustic molecular imaging agents in living mice. Nat Nanotechnol. 2008; 3:557–562. [PubMed: 18772918]
16. Wang LV. Multiscale photoacoustic microscopy and computed tomography. Nat Photonics. 2009; 3:503–509. [PubMed: 20161535]
17. Zavaleta CL, Kircher MF, Gambhir SS. Raman's "Effect" on Molecular Imaging. J Nucl Med. 2011
18. Keren S, et al. Noninvasive molecular imaging of small living subjects using Raman spectroscopy. Proc Natl Acad Sci U S A. 2008; 105:5844–5849. [PubMed: 18378895]
19. Zavaleta C, et al. Noninvasive Raman spectroscopy in living mice for evaluation of tumor targeting with carbon nanotubes. Nano Lett. 2008; 8:2800–2805. [PubMed: 18683988]
20. Zavaleta CL, et al. Multiplexed imaging of surface enhanced Raman scattering nanotags in living mice using noninvasive Raman spectroscopy. Proc Natl Acad Sci U S A. 2009; 106:13511–13516. [PubMed: 19666578]
21. Adiseshaiah PP, Hall JB, McNeil SE. Nanomaterial standards for efficacy and toxicity assessment. Wiley Interdiscip Rev Nanomed Nanobiotechnol. 2010; 2:99–112. [PubMed: 20049834]
22. Trehin R, et al. Fluorescent nanoparticle uptake for brain tumor visualization. Neoplasia. 2006; 8:302–311. [PubMed: 16756722]
23. Loening AM, Gambhir SS. AMIDE: a free software tool for multimodality medical image analysis. Mol Imaging. 2003; 2:131–137. [PubMed: 14649056]
24. Vivanco I, et al. The phosphatase and tensin homolog regulates epidermal growth factor receptor (EGFR) inhibitor response by targeting EGFR for degradation. Proceedings of the National Academy of Sciences of the United States of America. 2010; 107:6459–6464. [PubMed: 20308550]
25. Ermilov SA, et al. Laser optoacoustic imaging system for detection of breast cancer. J Biomed Opt. 2009; 14:024007. [PubMed: 19405737]
26. Manohar S, et al. Initial results of in vivo non-invasive cancer imaging in the human breast using near-infrared photoacoustics. Opt Express. 2007; 15:12277–12285. [PubMed: 19547596]
27. de la Zerda A, et al. Photoacoustic ocular imaging. Optics letters. 2010; 35:270–272. [PubMed: 20125691]
28. de la Zerda A, et al. Ultrahigh sensitivity carbon nanotube agents for photoacoustic molecular imaging in living mice. Nano letters. 2010; 10:2168–2172. [PubMed: 20499887]
29. de la Zerda A, Kim JW, Galanzha EI, Gambhir SS, Zharov VP. Advanced contrast nanoagents for photoacoustic molecular imaging, cytometry, blood test and photothermal theranostics. Contrast Media & Molecular Imaging. 2011; 6:346–369. [PubMed: 22025336]
30. Zuin S, et al. Weight of Evidence approach for the relative hazard ranking of nanomaterials. Nanotoxicology. 2010
31. Kircher MF, Gambhir SS, Grimm J. Noninvasive cell-tracking methods. Nat Rev Clin Oncol. 2011
32. Thakor AS, et al. The fate and toxicity of Raman-active silica-gold nanoparticles in mice. Sci Transl Med. 2011; 3:79ra33.
33. Thakor AS, et al. Oxidative stress mediates the effects of Raman-active gold nanoparticles in human cells. Small. 2011; 7:126–136. [PubMed: 21104804]
34. Zavaleta CL, et al. Preclinical Evaluation of Raman Nanoparticle Biodistribution for their Potential Use in Clinical Endoscopy Imaging. Small. 2011; 7:2232–2240. [PubMed: 21608124]
35. Maeda H, Wu J, Sawa T, Matsumura Y, Hori K. Tumor vascular permeability and the EPR effect in macromolecular therapeutics: a review. J Control Release. 2000; 65:271–284. [PubMed: 10699287]
36. Koljenovic S, et al. Raman spectroscopic characterization of porcine brain tissue using a single fiber-optic probe. Anal Chem. 2007; 79:557–564. [PubMed: 17222020]
37. Short MA, et al. Development and preliminary results of an endoscopic Raman probe for potential in vivo diagnosis of lung cancers. Opt Lett. 2008; 33:711–713. [PubMed: 18382526]

38. Nishimura, DG. Principles of Magnetic Resonance Imaging. Raleigh, NC: Lulu Publishers; 1996.
39. Graves EE, Quon A, Loo BW Jr. RT_Image: an open-source tool for investigating PET in radiation oncology. Technol Cancer Res Treat. 2007; 6:111–121. [PubMed: 17375973]
40. American National Standards Institute. ANSI Standard Z136.1-2000. New York: ANSI, Inc.; 2000. American national standard for the safe use of lasers.

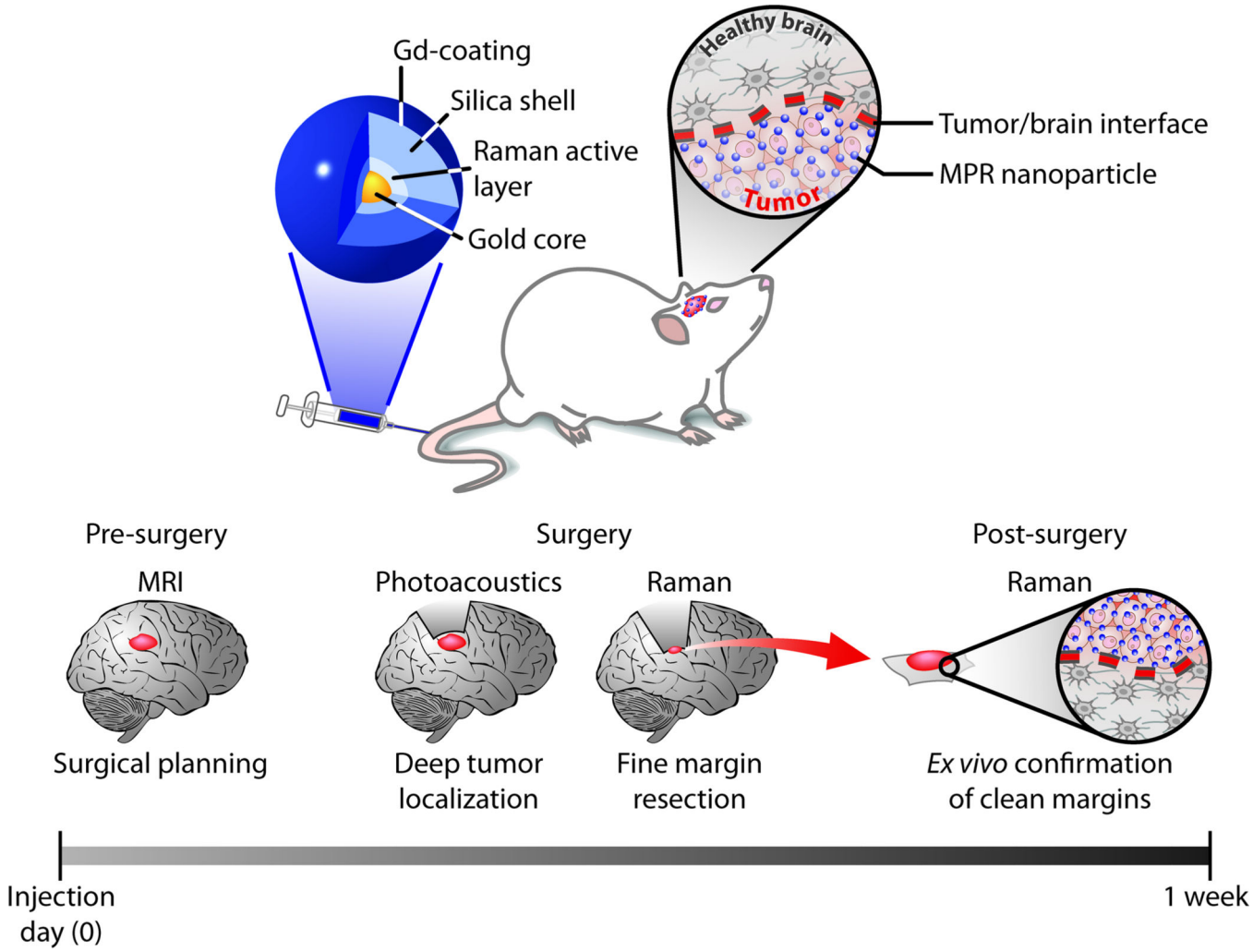

Figure 1. Triple-modality MPR concept

Top: MPRs are injected intravenously into a mouse bearing an orthotopic brain tumor. As the nanoparticles circulate in the blood stream, they diffuse through the disrupted blood-brain-barrier and are then sequestered and retained by the tumor. The MPRs are too large to cross the intact blood-brain-barrier and therefore cannot accumulate in healthy brain.

Bottom: Concept of proposed eventual clinical use. Detectability by MRI allows pre-operative detection and surgical planning. Due to the retention of the probe, only one injection is necessary and the probe can be detected in the tumor during surgery several days later. Photoacoustic imaging with its relatively high resolution and deep tissue penetration is then able to guide bulk tumor resection intra-operatively. Raman imaging with its ultrahigh sensitivity and spatial resolution can then be used to remove residual microscopic tumor burden. Resected specimen can subsequently be examined with a Raman probe *ex vivo* to verify clear margins.

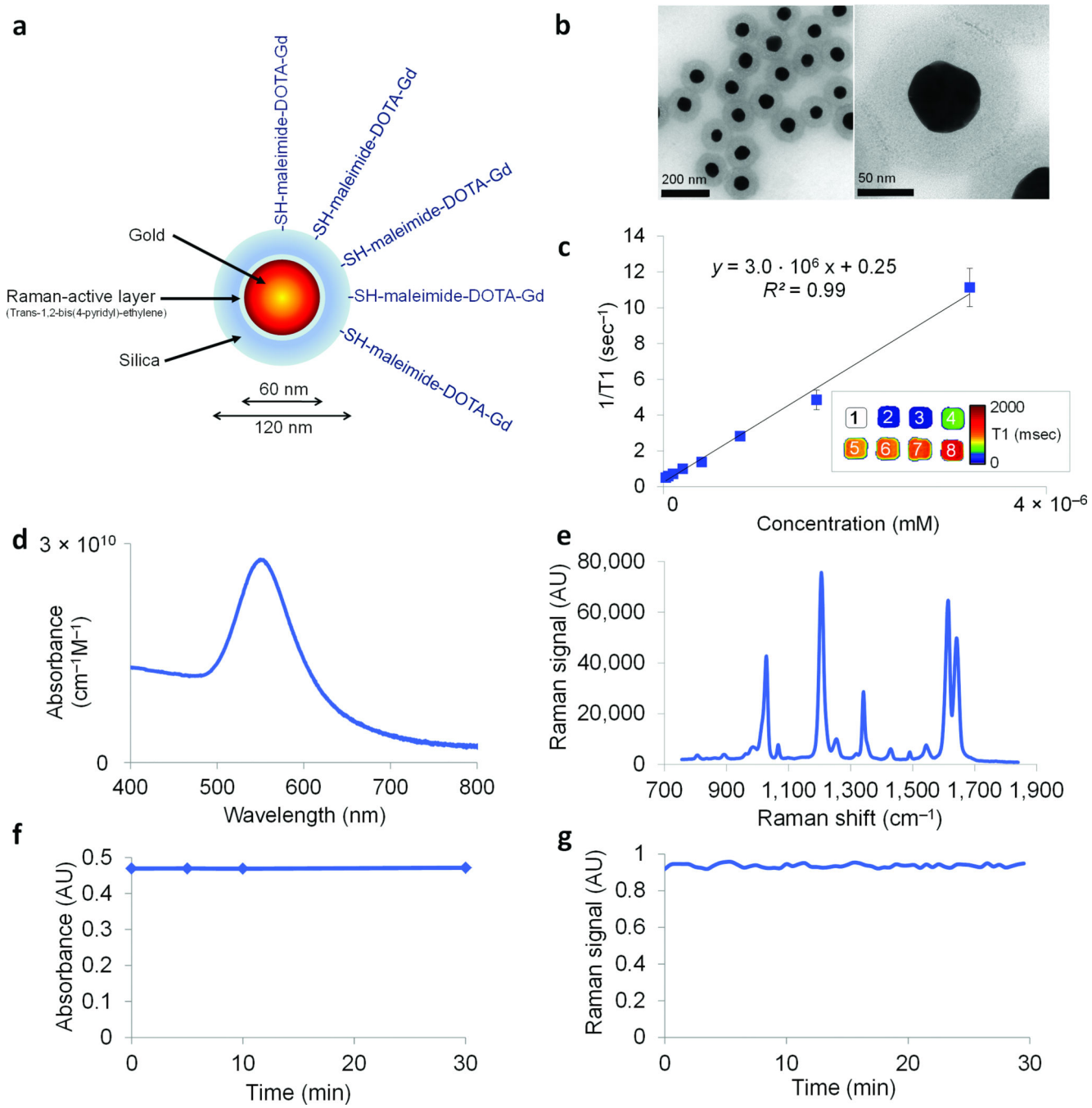

Figure 2. Characterization of the MPRs

a. Simplified diagram of the MPR. A 60 nm gold core is surrounded by a thin Raman active layer that is protected by a 30 nm silica coating. The silica coating was further functionalized with maleimide-DOTA-Gd, which was conjugated to the thiol group on the silica. **b.** Transmission electron microscopy images of MPRs. **c.** Particle relaxivity derived from T1 maps of probe dilutions in MRI phantoms. Data represent mean of two separate phantoms containing separate probe conjugations (error bars (s.e.m.) indicate batch-to-batch variation). Inset: T1 map of a MRI phantom containing MPRs at concentrations ranging

from 3.2 nM (1) to 25 pM (8). **d.** Optical absorbance of MPRs. **e.** Raman spectrum of MPRs with characteristic peaks at 1,021 cm^{-1}, 1,204 cm^{-1}, 1,340 cm^{-1}, 1,614 cm^{-1}, and 1,638 cm^{-1}. **f, g.** During 30 min of continuous laser irradiation, the optical absorbance (**f**) and the Raman signal (**g**) remained constant. AU, arbitrary units.

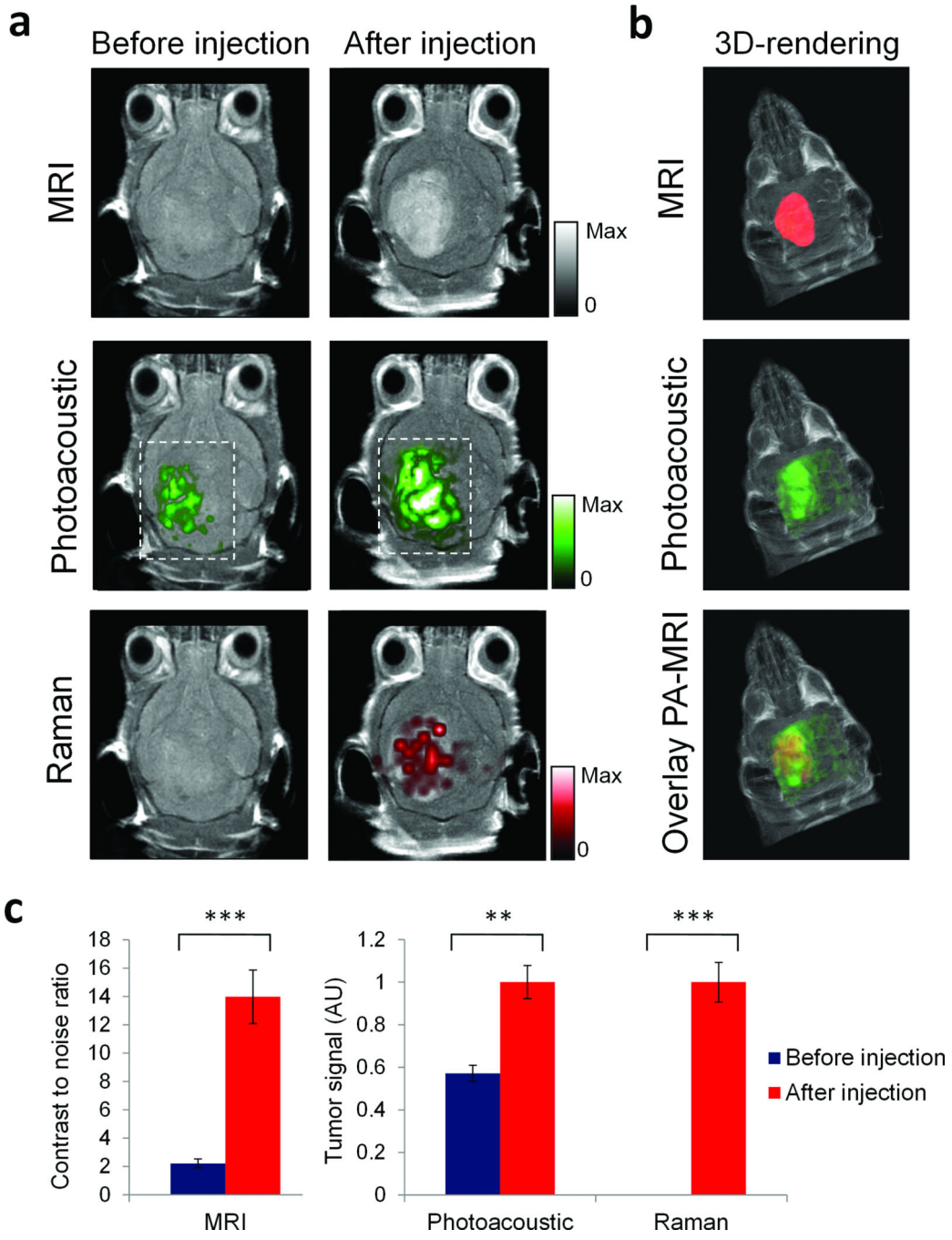

Figure 3. Triple-modality detection of brain tumors in living mice with MPRs

Three weeks after orthotopic inoculation, tumor-bearing mice (n = 4) were injected intravenously with MPRs (16 nM, 170 μl). Photoacoustic, Raman and MR images of the brain (skin and skull intact) were acquired before and 2 h, 3 h and 4 h after injection, respectively. **a.** 2D axial MRI, Photoacoustic and Raman images. The post-injection images of all three modalities demonstrated clear tumor visualization. The Photoacoustic and Raman images were co-registered with the MR image, demonstrating good co-localization between the three modalities. **b.** 3D-rendering of MR images with the tumor segmented (red;

top); overlay of 3D Photoacoustic images (green) over MRI (middle); and overlay of MRI, segmented tumor and Photoacoustic image (bottom) showing good co-localization of the Photoacoustic signal with the tumor. **c.** Quantification of signal in the tumor shows significant increase in MRI, Photoacoustic and Raman signals before versus after the injection ("***" indicates $P < 0.001$, "**" indicates $P < 0.01$). Error bars represent s.e.m. AU, arbitrary units.

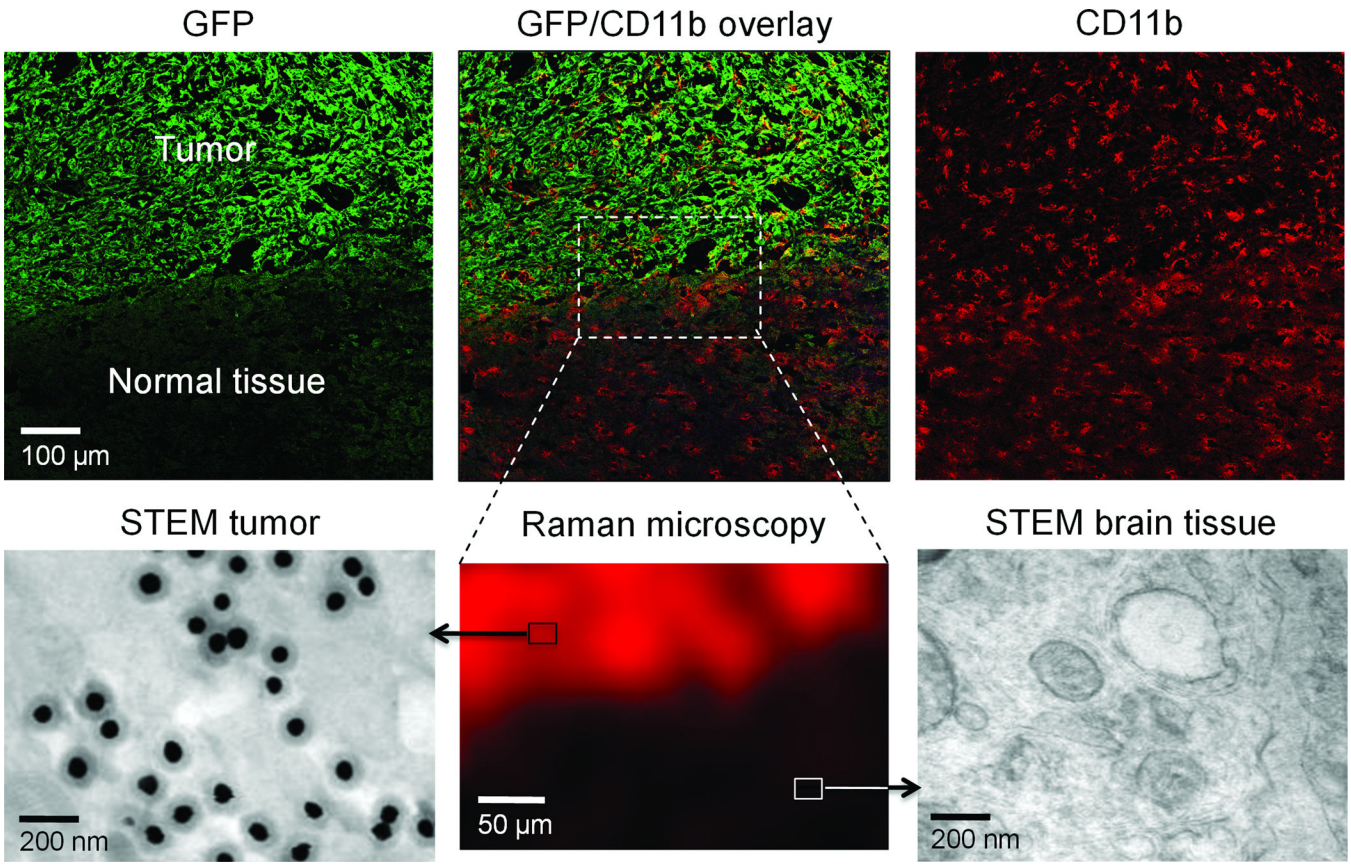

Figure 4. Histological validation

Upper row: 10 µm frozen sections from the margin of an eGFP$^+$U87MG brain tumor were stained for eGFP (green) to visualize the tumor margins and CD11b (red) to visualize glial cells and were examined by laser scanning confocal microscopy. **Bottom row:** A 50 µm adjacent slice was examined by Raman microscopy to visualize the distribution of the MPRs. Note the Raman signal corresponding to the eGFP$^+$ cells, indicating the presence of the probe in the tumor but not in the adjacent healthy tissue. The Raman signal (red) was scaled from 0 to 100 (AU). Boxes not drawn to scale. STEM images verified the presence of MPRs in the brain tissue, while no MPRs were seen in the healthy brain tissue. A three-dimensional STEM rendering of MPRs in brain tumor is provided in the Supplementary Information as Supplementary Movie.

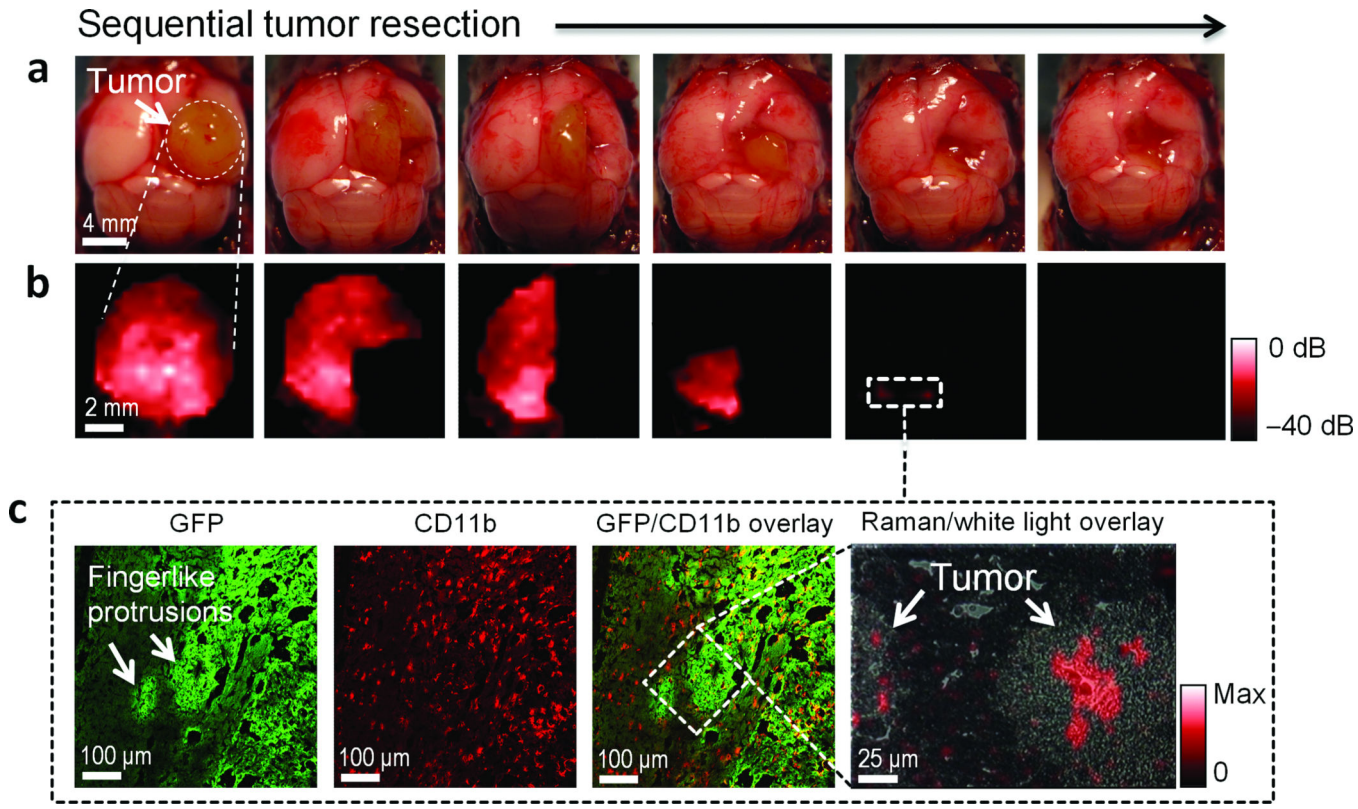

Figure 5. Raman-guided intra-operative surgery using MPRs

a. Living tumor-bearing mice (n = 3) underwent craniotomy under general anesthesia. Quarters of the tumor were then sequentially removed (as illustrated in the photographs) and **b.** intra-operative Raman imaging was performed after each resection step, until the entire tumor had been removed by visual inspection. After the gross removal of the tumor, several small foci of Raman signal were found in the resection bed (outlined by dashed white square; some Raman images smaller than black square). Raman color scale in red from −40 to 0 dB. **c.** Subsequent histological analysis of sections from these foci demonstrated an infiltrative pattern of the tumor in this location, forming finger-like protrusions extending into the surrounding brain tissue. As shown in the Raman microscopy image (right), Raman signal was observed within these protrusions, indicating the selective presence of MPRs in these protrusions. Box not drawn to scale. Raman signal in linear red color scale.